IN SITU HYDRATION IMAGING STUDY OF A YE'ELIMITE PASTE BY PTYCHOGRAPHIC X-RAY COMPUTED TOMOGRAPHY

Ana Cuesta[†], Angeles G. De la Torre[#], Isabel Santacruz[#], Pavel Trtik[§], Julio C. da Silva[§$], Ana Diaz[§], Mirko Holler[§], Miguel A. G. Aranda[†#]

[†] ALBA Synchrotron, Carrer de la Llum 2-26, E-08290 Cerdanyola del Vallès, Barcelona, Spain

[#] Departamento de Química Inorgánica, Cristalografía y Mineralogía, Universidad de Málaga, 29071-Málaga, Spain

[§] Paul Scherrer Institut, Villigen PSI, 5232, Switzerland

[$] Currently at European Synchrotron Radiation Facility, Grenoble, 38000, France.

email: acuesta@cells.es

ABSTRACT

Eco-cements are a desirable alternative to ordinary Portland cements because of their lower CO_2 footprints. For instance, the manufacture of Calcium SulfoAluminate (CSA) cements is more environmentally friendly than that of Portland cements as their production may decrease CO_2 footprint by up to 40%. CSA cements contain ye'elimite, $Ca_4Al_6O_{12}SO_4$, as main phase. The hydration of ye'elimite leads to hydrated compounds such as crystalline ettringite (AFt), crystalline monosulfoaluminate (AFm) and amorphous aluminum hydroxide gel, $Al(OH)_3 \cdot nH_2O$.

Here, we report the results of a ptychographic X-ray computed tomography (PXCT) study on the *in situ* hydration of ye'elimite with gypsum at different early ages. PXCT is a nondestructive X-ray imaging technique which provides 3D electron density and attenuation coefficient distributions of cement pastes with an isotropic resolution close to 100 nm allowing distinguishing between component phases with very similar contrast in more conventional absorption-based X-ray tomography. The sample was prepared by hydrating ye'elimite with gypsum. Four datasets were recorded at 48, 53, 58 and 63 hours of hydration. The main aim of this imaging study was to quantify the microstructure evolution, within this time interval, with submicrometer spatial resolution. The different component phases were identified and their mass densities determined. Furthermore, the tomograms were segmented and the volume percentage of each component were determined and compared at the four hydrating ages.

The overall porosity content (air and pore solution) decreased from 11.5 to 8.8 vol% and the anhydrous material content (ye'elimite and gypsum) decreased from 14.7 to 7.5 vol% in the studied time interval. Correspondingly, the hydrated content (crystalline ettringite and aluminum hydroxide gel) increased from 73.7 to 83.7 vol%.

The time evolution of several anhydrous particles was analyzed to determine the dissolution rate of the ye'elimite particles. Similarly, the pore filling process has also been investigated by quantifying their time evolution. These rates are reported and some insights about the mechanisms of these processes are discussed.

INTRODUCTION

Ye'elimite is the most important phase in calcium sulfoaluminate cements (CSA) (1) since it develops early mechanical strengths. CSA binders may have quite variable compositions, but all of them contain more than 50 wt% of ye'elimite phase, $Ca_4Al_6O_{12}SO_4$, also called Klein's salt or tetracalcium trialuminate sulfate as their main phase (2,3). They also have minor amounts of other phases such as belite, tetracalcium aluminoferrate, anhydrite, gehlenite or mayenite [4]. Ye'elimite is also present, ~25 wt%, in sulfobelite cements (5,6). CSA cements are very promising environmentally-friendly materials because they allow decreasing the CO_2 footprint of cement production. For every tonne of ordinary Portland cement (OPC) produced, ~0.97 tonnes of CO_2 are released into the atmosphere, with the cement industry contributing around 6% of all anthropogenic CO_2 emissions translating into approximately 4% of the planet's global warming (7). By comparison, CSA cements are produced with significantly lower CO_2 emissions relative to OPC, achieved through the use of lower amount of carbonated raw-materials (part of calcite is replaced by gypsum) and a reduced clinkering temperature (1). Moreover, CSA cements are also relatively friable after firing and consequently require less energy to be ground. The overall CO_2 emission reduction can amount up to 40% (8).

During the 1970s, CSA cements were introduced into the Chinese market as a result of the high-performing and dimensionally-stable cementitious matrices developed by China Building Materials Academy (9). However, in Europe, the use of CSA cements is limited by the lack of standards concerning special cements derived from non-Portland clinkers. Recently, the manufacture and marketing of CSA cements has been started by several European cement companies (2,10-12).

Ye'elimite hydrates very fast and most of the hydration heat is released during the first hours. Consequently, retarders are needed to ensure workability of the corresponding mortars and concretes (13). The hydration reaction of ye'elimite in presence of a sulfate source has been previously reported and it is shown in reaction [1], where the products are crystalline ettringite, $Ca_6Al_2(OH)_{12}(SO_4)_3 \cdot 26H_2O$ (also known as AFt) and amorphous aluminum hydroxide (also known as aluminum hydroxide gel, A-H gel or amorphous gibbsite) (14,15).

$$Ca_4Al_6SO_{16} + 2CaSO_4 \cdot nH_2O + (38-2n)\,H_2O \rightarrow Ca_6Al_2(OH)_{12}(SO_4)_3 \cdot 26H_2O + 4Al(OH)_3\text{-gel} \quad [1]$$

X-ray tomography has become an important tool for investigating Portland cement hydration to study the pore network, tortuosity and other relevant parameters (16,17). In addition, *in situ* hydration studies have been also performed in cement pastes by X-ray tomography. *In situ* studies are important to control the reaction kinetics and the microstructure of the hydration products in spite of using protocols to stop the hydration which can alter the microstructure. The hydration of a Portland cement from 1 to 60 days was studied *in situ* by synchrotron X-ray microtomography (18). However, the study of the hydration mechanism was limited due to the low spatial resolution which did not allow resolving the small pores and particles. An X-ray absorption tomographic study focused on the characterization of OPC and CSA pastes was also reported (19). The study was based on the study of the morphological evolution of mineral phases and the analyses of the three-dimensional evolution of the pore network up to 12 hours. Moreover, a very recent *in situ* study was devoted to the evolution of the gypsum plaster setting in order to study the hydration kinetics and the final microstructure of gypsum. A thorough study was performed for different particles in order to determine the dissolution speed of the hemihydrate as a function of the particle thickness (20). It is important to point out that a review about the use of synchrotron radiation to investigate cements has also been reported. That review includes an overview of the available imaging approaches (21).

Additionally, ptychographic X-ray computed tomography (PXCT) is a scanning microscopy technique which uses the coherence properties of synchrotron radiation (22). In PXCT, the post-sample X-ray optics is replaced by phase retrieval algorithms which, combined with the ptychographic approach, make the technique very reliable and robust (22-26). A confined X-ray beam is used to illuminate the sample and coherent diffraction patterns are recorded in the far field from different overlapping illumination regions of the sample. Finally, the amplitude and the phase of the complex-valued transmissivity of the sample can be obtained due to the redundancy in the data and the use of iterative phase retrieval algorithms. This technique provides 2D high-resolution projections of the sample and a three-dimensional distribution of the difference from unity of real part of the refractive index, $\delta(\mathbf{r})$, and the imaginary part of the index, $\beta(\mathbf{r})$, can be simultaneously obtained when applying a tomographic approach. Moreover, PXCT can provide isotropic 3D resolution better than 20 nm (27) and, if the stoichiometries are known, accurate mass density values. (28)

The 3D electron density distribution, $n_e(\boldsymbol{r})$, can be obtained as (28)

$$n_e(\boldsymbol{r}) = \frac{2\pi\delta(\boldsymbol{r})}{r_0\lambda^2} \qquad [2]$$

where r_o is the electron radius and λ is the X-ray wavelength. PXCT provides quantitative information for materials of known chemical composition. In this case, the mass density can be calculated as (28)

$$\rho(\boldsymbol{r}) = \frac{n_e(\boldsymbol{r})A}{N_A Z} \qquad [3]$$

where N_A is Avogadro's number, A is the molar mass, and Z is the total number of electrons in the formula unit.

The measure of the mass densities of every component within complex matrices with a high sensitivity and selectivity makes the technique very appropriate for studying the microstructures of cement pastes (29,30). PXCT was applied to investigate the hydration of an OPC. The composition, density and microstructure of all their components were studied (29). Furthermore, the 3D tomograms were segmented and the mass densities of the different phases were quantitatively determined. This technique was also used to image the hydration of alite, the main phase of OPC. In this case, the densities and water contents of C-S-H gels were determined (30). Finally, ye'elimite-containing pastes have been recently investigated by PXCT. All the phases were segmented and the composition and mass density of aluminum hydroxide gels were determined (31).

In this work, PXCT has been used to perform an *in situ* study of a ye'elimite-containing paste. The mass densities of the different phases have been determined. In addition, the tomograms have been segmented and the volume percentages have been determined and compared at four different ages. Finally, the evolution of the dissolution of some anhydrous ye'elimite particles with the hydration time has been also characterized.

EXPERIMENTAL SECTION

Sample preparation.

A stoichiometric mixture of ye'elimite (32) and gypsum was prepared according to reaction [1]. The starting anhydrous mixture was milled for 40 minutes in a vibratory mill and after that, it was attrition milled with isopropanol for 30 minutes (3 cycles of 10 minutes) to ensure that large

particles could not block the narrow parts of the capillaries. Then, to prepare the paste for the PXCT experiment the appropriate amount of the mixture was weighted. The mixture was loaded inside a tapering quartz capillary using an ultrasound bath to shake the capillary for the powder to reach the tip. Afterwards, the capillary was filled up with the appropriate amount of distilled water with a water-to-solid (w/s) ratio of 1.4, and immediately both ends of the capillary were sealed with UV-hardening glue. The sample was stored at room temperature (RT).

PXCT experiments and data processing.

The measurements were carried out at the cSAXS beamline at the Swiss Light Source, Paul Scherrer Institut, Villigen, Switzerland, using the instrumentation described elsewhere (27,33) which uses laser interferometry for accurate positioning of the specimen with respect to the beam-defining optics (34). The energy of the X-ray photons was set to 6.2 keV using a Si(111) monochromator. A coherently illuminated gold Fresnel zone plate (35) of 170 μm diameter, outermost zone width of 60 nm, and 51 mm focal length was used to define the illumination onto the sample. The sample was placed at 2.6 mm from the focus in order to obtain an illumination spot of 8.7 μm in diameter on the sample. The far-field diffraction patterns were acquired with the detector EIGER 500k (36) with a pixel size of 75 μm which was placed at 7.35 m distance from the sample, satisfying the ptychography sampling conditions (37,38). Each ptychographic scan spanned a field of view of 72 microns times 45 microns (horizontal x vertical) and consisted of about 360 positions following the pattern of a Fermat spiral (39) with a step size of 3 μm and, at each step, a coherent diffraction pattern was acquired with 0.1 s of exposure. From each diffraction pattern, only a region of 400×400 pixels of the detector area was used for ptychographic reconstructions, which resulted in a pixel size of 40.8 nm in the reconstructed images. The tomographic projections were acquired using a binary acquisition strategy with 8 interlaced nests of projections as described by Kaestner et al. (40). Finally, 600 projections at equally spaced angular intervals within the angular range of 0° and 180° for the sample were obtained. The total acquisition time for the complete tomographic dataset, including the time needed for sample positioning and other possible overhead of the measurement was approximately 20 h. The final projections were divided and reconstructed in four different sub-tomograms (5 h each) at the average corresponding hydration ages, 48, 53, 58 and 63 hours. We estimate that the total dose imparted on the specimen ranged from about 1.4×10^7 Gy for the A-H gel to 3.9×10^7 Gy for ye'elimite for all 600 projections.

During the ptychographic phase retrieval for each projection, some projections still exhibited non-physical phase vortices after 1600 iterations of the difference map algorithm, (41) which typically indicates that the final convergence of the algorithm has not been achieved yet. Thus, in order to assist the convergence, we pushed the reconstructions away from such stagnation point doing the following: i) the vortex positions and their corresponding topological charges were found in each projection using the procedure explained in Goldstein et al.; (42) ii) the vortices were removed by a product with a phase vortex of opposite topological charge at the same positions; iii) the reconstructions were then casted into further 500 iterations of the difference map algorithm until the proper convergence was reached. Finally, 100 iterations of maximum-likelihood optimization (43) were applied to the reconstructions.

The phase projections needed to undergo several processing steps including the removal of zero and 1^{st} linear terms, phase unwrapping, and vertical alignment (44) prior to the tomographic reconstruction. In addition, the horizontal alignment of the projections was performed using a tomographic consistency approach (45). Finally, we applied a modified filtered backprojection (FBP) suitable for wrapped phase (44) using a Hanning filter with 0.2 normalized cut-off frequency, taking into account its higher signal-to-noise ratio. The spatial resolution of the 3D

images of the phase contrast tomogram was determined using the Fourier Shell Correlation (FSC) method with a threshold based on the half-bit criterion (27,46).

Segmentation of the material phases.

The segmentation study was carried out to determine the volume of the different component phases. The segmentation study was performed with Avizo® Fire edition v. 8.0 (FEI Visualization Sciences Group). A region of interest, excluding the capillary, was selected to perform threshold-based image segmentation on the phase contrast tomogram. The materials were separated using the average values obtained for the electron densities by applying the threshold tool which is included in the segmentation editor of the Avizo suite®. The volume percentages of each component phase were quantitatively determined using the tool "material statistics" of the Avizo suite®.

RESULTS AND DISCUSSION

PXCT generates two tomographic data sets: the 3D electron density distribution, $\mathbf{n_e(r)}$, obtained from the phase projections, and the 3D distribution of the complex-part or the refraction index, $\boldsymbol{\beta}\mathbf{(r)}$, obtained from the absorption projections. For this study, only the 3D electron density distribution tomograms were used due to their higher spatial resolution.

The hydration kinetics of ye'elimite with gypsum has been investigated by PXCT at 48, 53, 58 and 63 hours of hydration. The volume of each reconstructed data set was about 1.5×10^5 μm^3. The 3D spatial resolution, determined by FSC, was estimated to be close to 500 nm. The resolution of the reconstructions is limited by the number of projections, the signal-to-noise ratio and also by the possible movement of the sample during the acquisition time. Figure 1 displays the same vertical slice of the tomogram at four different times. The phases have been labeled in the first tomogram, top left corner. Here, different components were identified based on their electron densities. Particles of anhydrous materials, gypsum and ye'elimite could be observed in the tomograms. Hydrated material phases such as crystalline ettringite and amorphous aluminum hydroxide gel were also identified. Finally, it is important to highlight the presence of a significant amount of air porosity and volume regions with a density close to that of water (pore solution).

PXCT gives quantitative information of the different component phases. For this reason, ten particles were analyzed for each component phase to determine their electron densities, which were converted to mass densities by using equation [3]. Good agreement between the measured and theoretical mass densities was found. No variations in the densities with time were obtained. Consequently, results are reported only for the 63 hour tomogram. Table 1 gives the average electron and mass densities obtained by PXCT. For the amorphous aluminum hydroxide gel, the chemical composition obtained in a previous study for a similar sample (31), $Al(OH)_3 \cdot 2.3H_2O$, was used for the determination of its mass density. In Table 1, the term pore solution is used to describe the water which is dissolving relevant chemical species (f.i. Ca^{2+}, SO_4^{2-}, etc.).

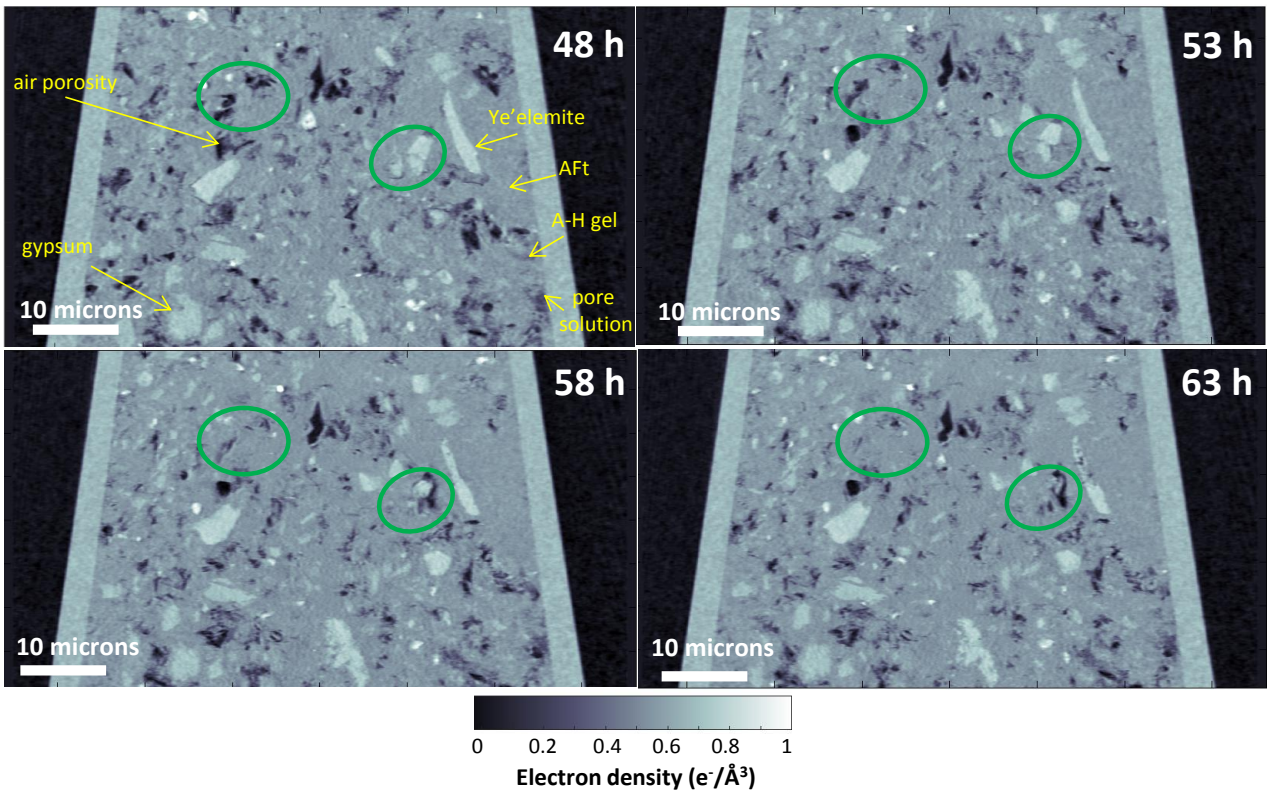

Figure 1. Vertical slices of the electron density tomograms from PXCT for ye'elimite with gypsum paste at the different ages.

Table 1. Electron and mass densities obtained by PXCT at 63 hours. Expected electron and mass densities are also listed for the sake of comparison.

Material phase	**Chemical Formula**	n_e/e⁻·Å^{-3}	**Expected electron density /e⁻·Å^{-3}**	**Measured mass density /g·cm^{-3}**	**Expected mass density /g·cm^{-3}**
pore solution	*≈H_2O*	0.36(1)	0.33 *(water)*	1.1(1)	1.00 *(water)*
A-H gel	$Al(OH)_3 \cdot 2.3H_2O$	0.46(1)	*0.74 (cryst. Gibb)*	*1.45(3)**	*2.40 (cryst. Gibb)*
AFt	$Ca_6Al_2(OH)_{12}(SO_4)_3 \cdot 26H_2O$	0.558(9)	0.56	1.77(2)	1.78
gypsum	$CaSO_4 \cdot 2H_2O$	0.701(4)	0.71	2.28(1)	2.30
ye'elimite	$Ca_4Al_6O_{12}SO_4$	0.767(7)	0.78	2.58(2)	2.60
capillary	SiO_2	0.673(7)	0.66	2.25(2)	2.20

* This number has been obtained by assuming the following stoichiometry, $Al(OH)_3 \cdot 2.3H_2O$, for the aluminum hydroxide gel (31).

In the first tomogram, at 48 h, a relatively large amount of porosity (both air and water) is clearly visible, see Figure 1. Moreover, we can observe the evolution of porosity, anhydrous particles and hydrated material such as aluminum hydroxide gel and ettringite with time. Some pores and anhydrous particles disappear with time leading to the formation of more hydrated material (Figure 1, green circles). This will be quantified below. The different electron densities of the components allow us to follow the evolution of the anhydrous phases, the hydrated products and the porosity during the hydration reaction.

The electron density histograms of a cubic volume-of-interest (VOI) inside the capillary of about 1.4×10^4 μm^3 (a cube size of $24\times24\times24$ μm^3) were computed at the four different ages and are displayed in Figure 2a as colored solid line in logarithmic scale to emphasize low content components. It is evident in the histogram the relatively high porosity of this sample. In the histograms, the distinction between hydrates, ettringite and aluminum hydroxide gel, is not possible due to the limited spatial resolution and the similarity of the electron density coefficients. The electron density histograms at early ages have been compared with that obtained for a sample hydrated for 18 days, which was previously reported (31). The starting materials were the same in both cases, but the w/s ratio in the scanned regions of these two samples does not necessarily has to be the same. For this second sample, the hydration reaction had finished and the obtained 3D resolution was far better, 140 nm. The hydrated materials, aluminum hydroxide gel and crystalline ettringite could be clearly distinguished, as well as air and water porosity (see dashed line in Figure 2a). Figure 2b displays the histograms in linear scale at 48 and 63 hours, the inset enlarges the region of the anhydrous phase peaks. The histogram for the first tomogram indicates a smaller number of voxels for the hydrated phases and higher amounts of anhydrous phases in comparison with the tomogram at 63 hours. Moreover, the electron density peaks in the histogram at 63 hours are better defined so that the evolution of the hydration reaction at that time is slower and consequently this tomogram, recorded in exactly the same conditions, has slightly better resolution.

Threshold-based image segmentation was performed at the different ages for a large VOI of about 5×10^4 μm^3 of the electron density tomogram. In each case, three different components were segmented and quantified: i) the component(s) with electron densities lower than 0.42 $e^-\cdot Å^{-3}$ were considered porosity (including pore solution and air pores); ii) hydrated phases were computed for electron densities ranging from 0.42 to 0.62 $e^-\cdot Å^{-3}$ (including aluminum hydroxide gel and crystalline ettringite); iii) anhydrous materials were calculated for electron densities higher than 0.62 $e^-\cdot Å^{-3}$. Volume percentages for different ages are displayed in Table 2. Moreover, a 3D rendering of a cut of the tomogram at each hydration time is shown in Figure 3. This figure displays the evolution of the hydration with time. Table 2 and Figure 3 show how the porosity slowly disappears as more hydrated material is formed partly filling these volumes. The dissolution of anhydrous particles can also be observed. A decrease by 2.7 vol% of the total volume of porosity was observed between the first and the last recorded tomogram. This is clearly linked to the formation of more hydrated material that fills this porosity. Moreover, the anhydrous material decreased by 7.2 vol%.

Table 2. Component contents (expressed in volume percentages) determined by PXCT for the analyzed paste at the different hydration ages.

Material phase (vol%)	Hydration time			
	48 h	53 h	58 h	63 h
Anhydrous (ye'elimite + gypsum)	14.7	10.0	8.0	7.5
Hydrated (AFt + A-H gel)	73.7	79.5	82.6	83.7
Total porosity	11.5	10.4	9.4	8.8

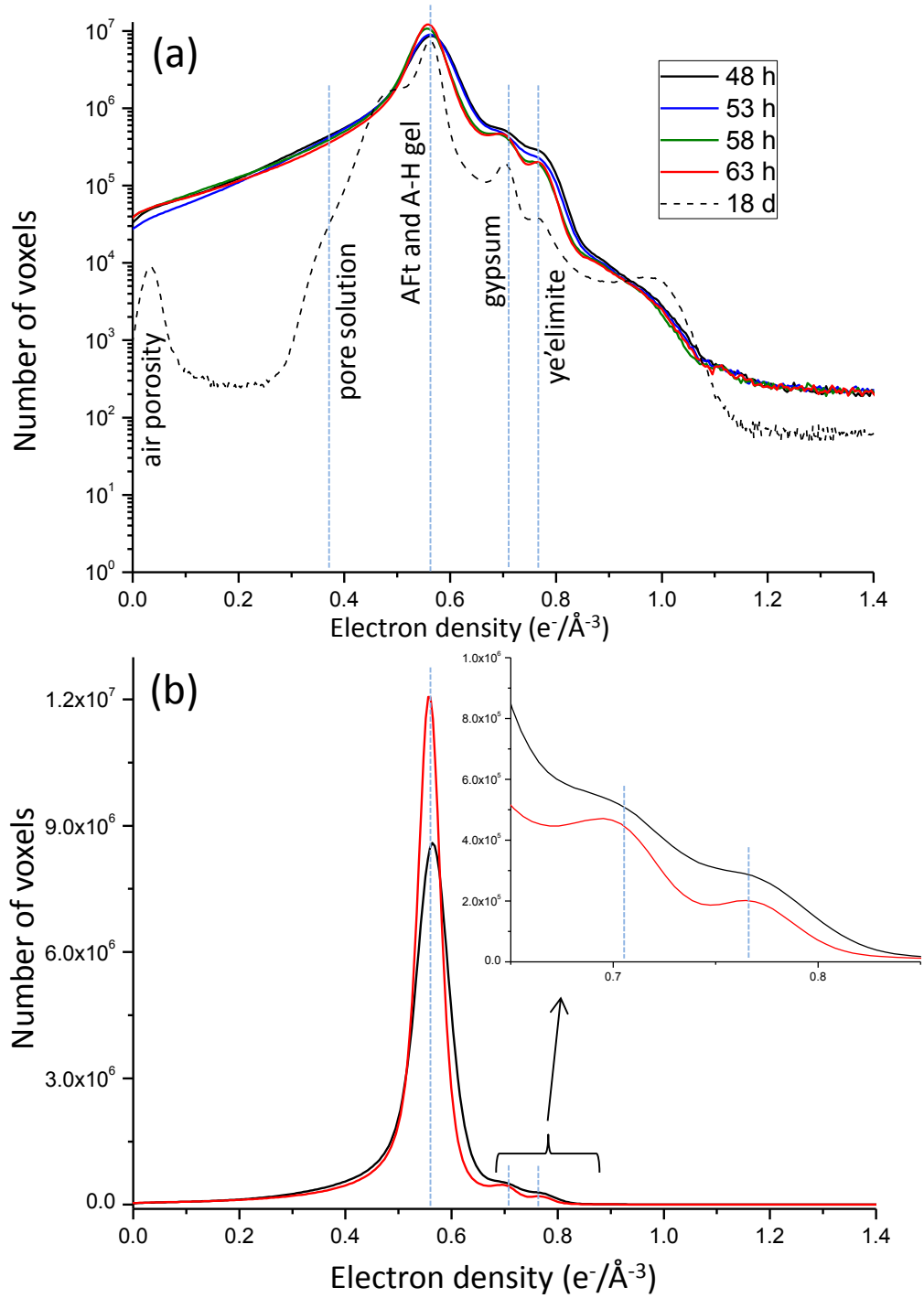

Figure 2. Volume-of-interest histogram of the electron densities for the sample in (a) logarithmic scale at the different hydration times and (b) linear scale at 48 (black) and 63 hours (red). The inset in (b) enlarges the region of anhydrous content.

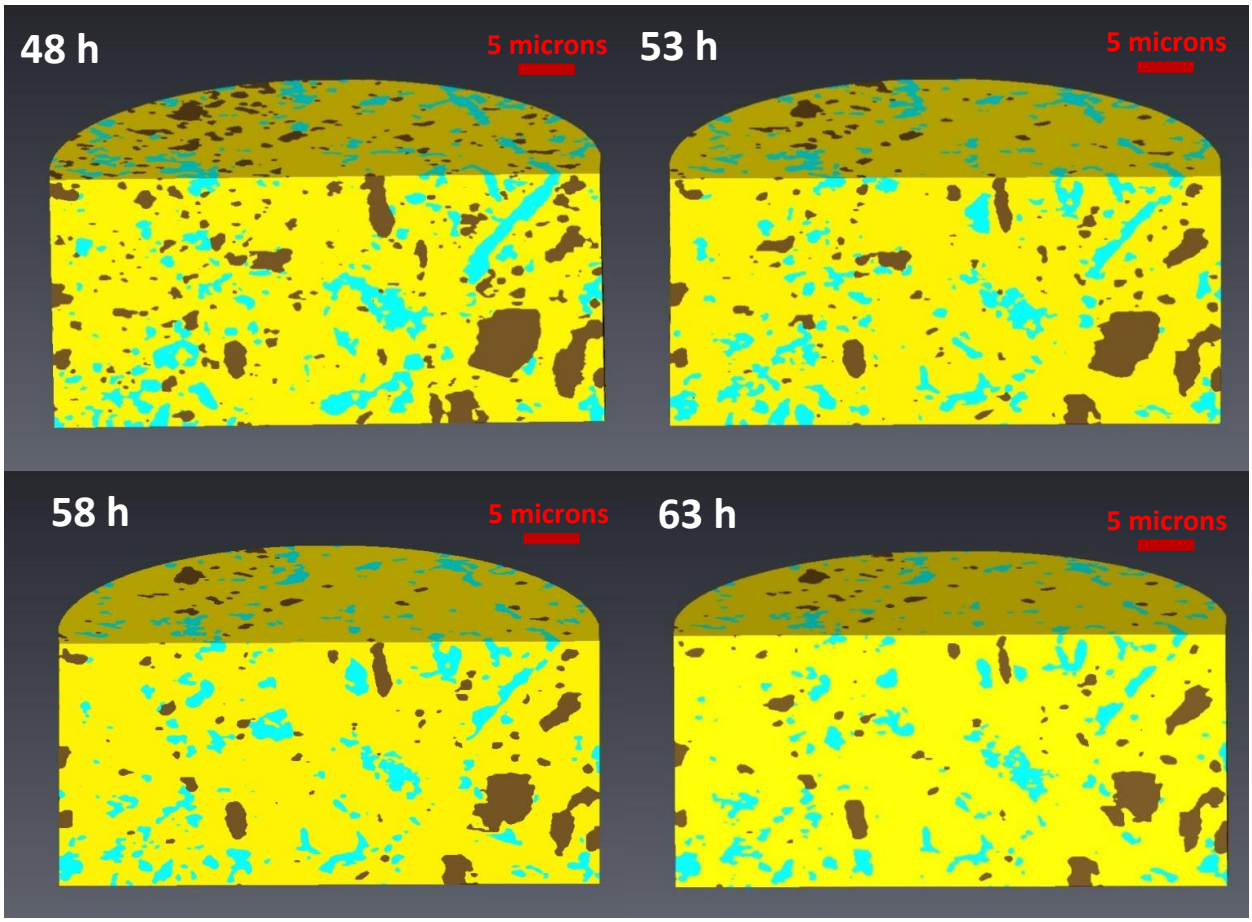

Figure 3. 3D renderings of the segmented volumes showing the material components of the same sample at different ages. Color codes: yellow for hydrated components (AFt and A-H gel); brown for anhydrous components (ye'elimite and gypsum); and light blue for total porosity.

The time evolution of selected volumes was closely followed. Firstly, several anhydrous particles were chosen and their dissolution rates were studied. This analysis was performed by monitoring the evolution of the electron density value across the particles with hydration time. This characterization was processed with ImageJ/Fuji shareware (47,48). Figure 4 presents the evolution of the electron density for two selected (anhydrous) ye'elimite particles jointly with the corresponding images of the particles. In the first case, the dissolution of the particle led to the formation of some air porosity and, at the same time, the hydrated material was also precipitating around the particle, see Figure 4 (top). However, this selected particle was not fully dissolved between 48 and 63 hours. Conversely, Figure 4 (bottom) shows a similar study for an anhydrous particle which dissolved completely. Both profiles show that the main differences for the dissolution of these particles can be found between 53 and 58 hours. The evolution with time was carried out for around 10 ye'elimite particles which were dissolving between 48 and 63 hours. It is important to highlight that other particles were not dissolved during this analyzed time period, see below. For the anhydrous particles, which were being dissolved, a dissolution speed could be determined using the difference in the measured particle thickness between 48 and 63 hours. In this case it was found that the average value for the ye'elimite dissolution rate, in this time period, was ~2 $nm \cdot min^{-1}$. The different morphologies of the particles showed that the hydration may well have started before 48 hours. It is evident from the analysis of the studied particles, see also Figure 4,

that the particles dissolved if the surfaces are close to pore solution which has an electron density smaller than ~0.45 $e^{-}\cdot Å^{-3}$. In addition, it was found that the dissolution of the particles was not regular along all the particle surfaces.

Secondly, some anhydrous ye'elimite particles were not dissolved within the studied period of time. Figure 5 shows the time evolution of two ye'elimite particles exhibiting this behavior. It can be seen that the electron density of the matrix which surround these particles is close to ~0.50 $e^{-}\cdot Å^{-3}$ or even higher. These values are higher than those expected for pore solution and they correspond to ettringite and aluminum hydroxide gel. Hence, we conclude that these particles do not dissolve because the water (pore solution) content close to the particles was quite low which does not allow mass transport.

Thirdly, the evolution of the air porosity was also followed. The electron density profiles for selected small pores were measured at the different hydration ages, see Figure 6. It is important to highlight that the electron density of the air porosity should be 0 but the small variations found are within the errors of the measurements. Figure 6 shows that the air pores are being filled with the hydrated phases. Moreover, the precipitation speed could be also determined based on 5 different pores of similar size of 2-3 micron diameter. It was found that the average value for the precipitation rate of hydrated phases in the studied time period was ~1 $nm\cdot min^{-1}$.

From this study, some insights about the hydration mechanism of ye'elimite-containing cements can be deduced: I) The measured ye'elimite dissolution rate, ~2 $nm\cdot min^{-1}$ seems faster than the hydrated precipitation rate, ~1 $nm\cdot min^{-1}$. II) Porosity develops close to the volume previously occupied by the dissolving anhydrous particles. III) The hydrated material partly occupied the initial volume of the anhydrous particles but it also fills the existing pores. IV) Some anhydrous ye'elimite particles were not dissolved within this period of time pointing towards a slightly inhomogeneous water distribution.

Finally, it is important to clarify that additional work is required to fully characterize the evolution of the ye'elimite/gypsum paste with time. PXCT allows us to monitor the *in situ* hydration of a cement sample with good spatial resolution, close to 500 nm, although the time required for obtaining the tomogram limits this type of experiments. However, instrumental developments, including upcoming diffraction-limited synchrotron sources, are expected to shorten this acquisition time. It is important to have a good spatial resolution, in order to be able to distinguish between pore solution, hydrated components and anhydrous material, but also with better temporal resolution. In any case, it is worth emphasizing that although the sample moves during acquisition, as the hydration reaction progresses, the ptychographic reconstruction algorithms converge within the required resolution, because these changes are small compared to the resolution within a single projection acquisition. On the other hand, changes occurring during an entire tomographic acquisition results in averaged microstructural information over the acquisition time.

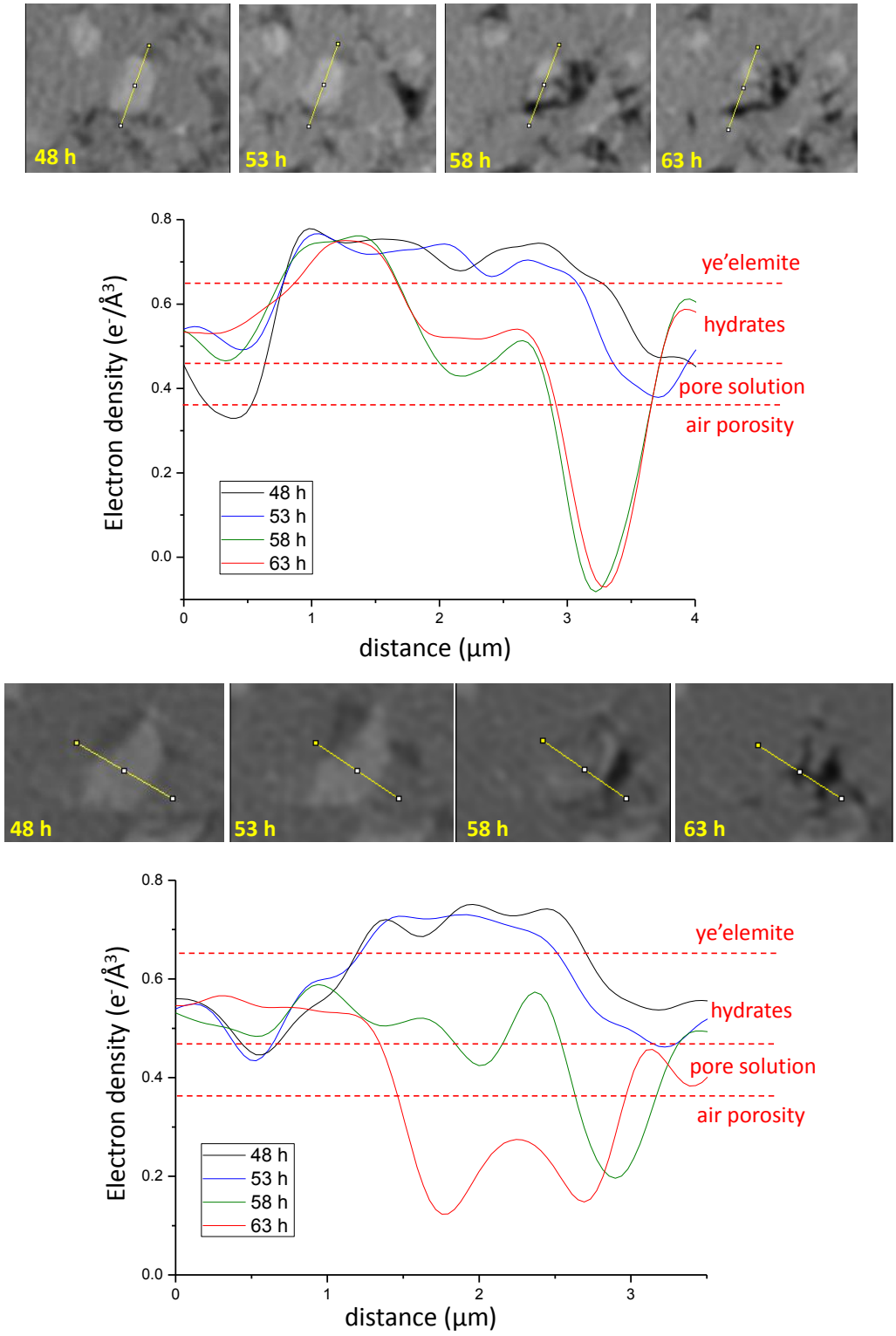

Figure 4. Electron density profile along the yellow line taken at the different hydration ages for two selected anhydrous ye'elimite particles which are being dissolved with time.

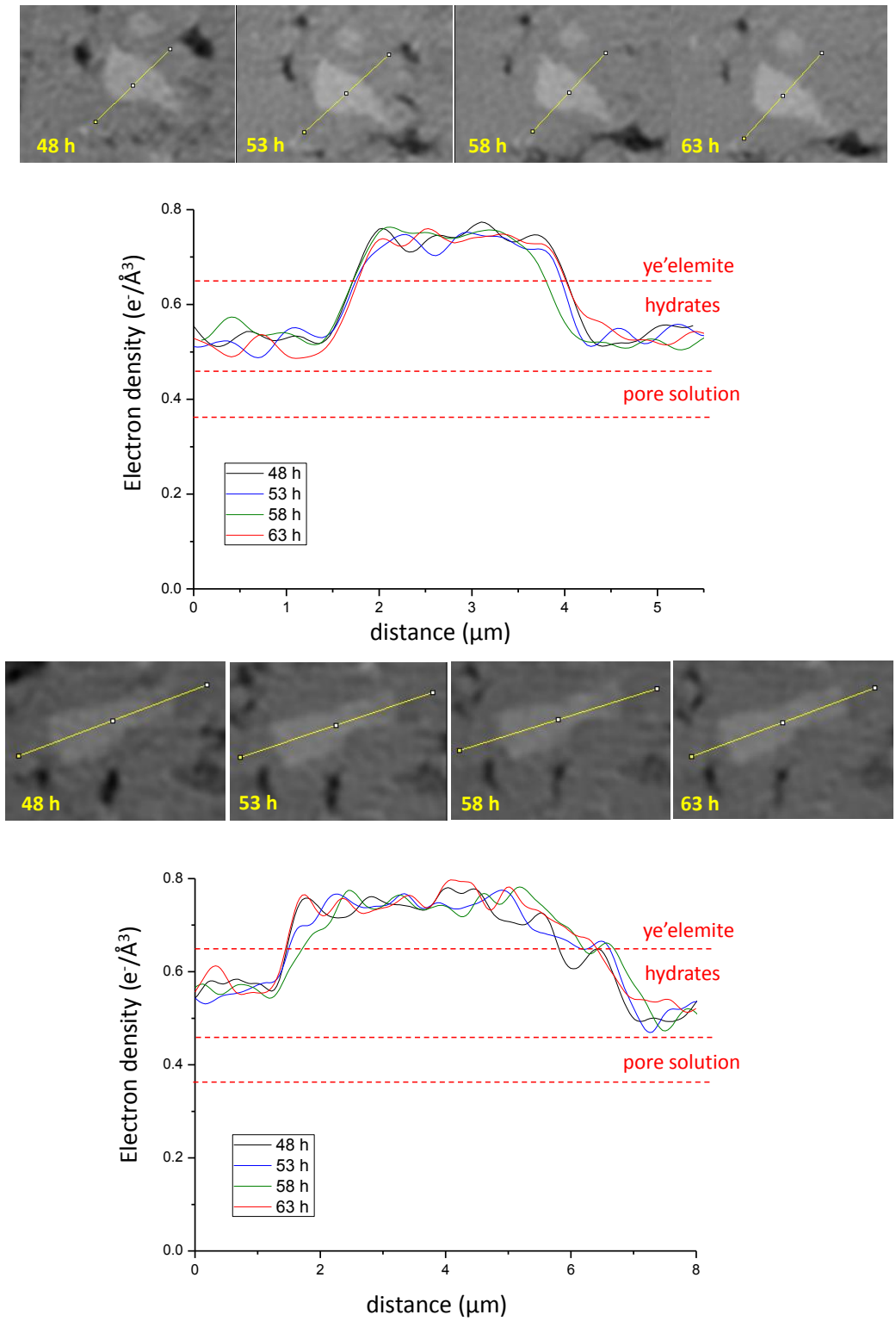

Figure 5. Electron density profile along the yellow line taken at the different hydration ages for two selected anhydrous ye'elimite particles which are not being dissolved with time.

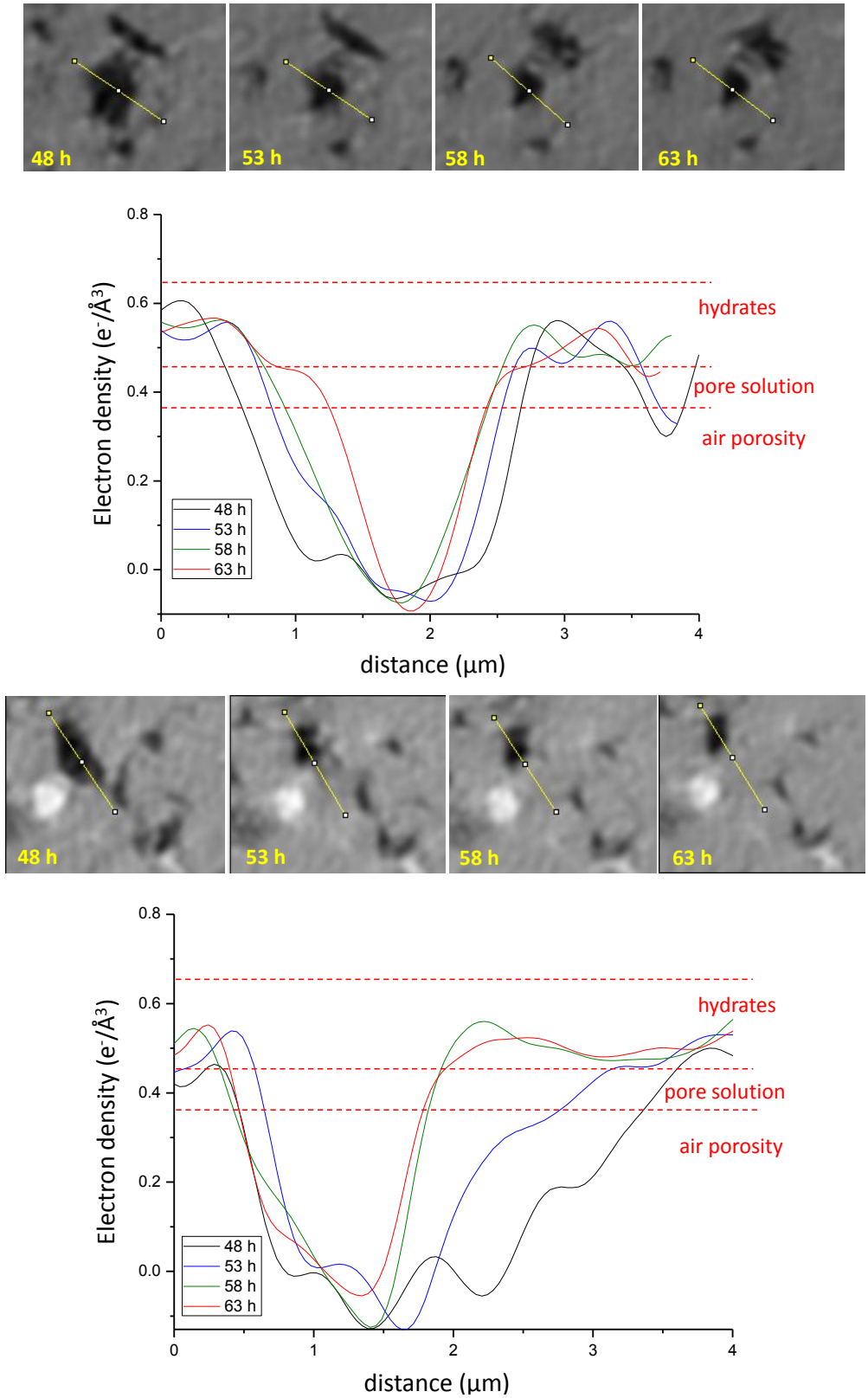

Figure 6. Electron density profile along the yellow line taken at the different hydration ages for two selected air-containing pores.

CONCLUSIONS

Ptychographic X-ray computed tomography has been used to perform an *in situ* microstructural study of a ye'elimite hydrating paste. Four datasets were collected at 48, 53, 58 and 63 hours of hydration time. In this study, it was possible to identify all the different component phases present in the paste. The mass densities of the different components such as anhydrous ye'elimite and gypsum, hydrated crystalline ettringite, and aluminium hydroxide gel were accurately determined. Segmentation of the tomograms showed the evolution of the hydration reaction with time. The volume percentage of anhydrous materials and porosity decreased with time leading to the formation of more hydrated material. Finally, the dissolution rate was determined to be ~2 $nm \cdot min^{-1}$ for some ye'elimite particles, while the precipitation rate was determined as ~1 $nm \cdot min^{-1}$ for the formation of ettringite and aluminium hydroxide gel within the pores.

REFERENCES

(1) Glasser F.P., Zhang L., High-performance cement matrices based on calcium sulphoaluminate-belite compositions, Cem. Concr. Res. 31 (2001) 1881-1886.

(2) Gartner E., Industrially interesting approaches to ''low-CO_2'' cements, Cem. Concr. Res. 34 (2004) 1489-1498.

(3) Odler I., Special Inorganic Cements, Taylor and Francis, London, 2000.

(4) Sahu S., Majling J., Phase compatibility in the system CaO–SiO_2–Al_2O_3–Fe_2O_3–SO_3 referred to sulphoaluminate belite cement clinker, Cem. Concr. Res. 23 (1993) 1331-1339.

(5) Álvarez-Pinazo G., Santacruz I., León-Reina L., Aranda M.A.G., De la Torre A.G., Hydration Reactions and Mechanical Strength Developments of Iron-Rich Sulfobelite Eco-cements, Ind. Eng. Chem. Res. 52 (2013) 16606-16614.

(6) Morin V., Walenta G., Gartner E., Termkhajornkit P., Baco I., Casabonne J.M., Hydration of a Belite-Calcium Sulfoaluminate- Ferrite cement: Aether^{TM} , Proceedings of the 13th international Congress on the Chemistry of Cement, Madrid, Spain, 2011.

(7) Flatt R.J., Roussel N., Cheeseman C.R., Concrete: An eco material that needs to be improved, J. Eur. Ceram. Soc. 32 (2012) 2787-2798.

(8) Aranda M.A.G., De la Torre A.G., Calcium sulfoaluminate cements and concretes, in *Eco-efficient concrete*; Ed. F. Pacheco-Torgal, Ed. S. Jalali, Ed. J. Labrincha, Woodhead Publishing: Cambridge, 2013, pp. 488-522.

(9) Zhang L., Su M., Wang Y., Development of the use of sulpho-and ferroaluminate cements in China, Adv. Cem. Res. 11 (1999) 15-22.

(10) Li G.S., Walenta G., Gartner E.M., Formation and hydration of low-CO_2 cements based on belite, calcium sulfoaluminate and calcium aluminoferrite, Proceedings of the 12th ICCC, Montreal, Canada, 2007.

(11) Juenger M.C.G., Winnefeld F., Provis J.L., Ideker J.H., Advances in alternative cementitious binders, Cem. Concr. Res. 41 (2011) 1232-1243.

(12) Álvarez-Pinazo G., Cuesta A., García-Maté M., Santacruz I., Losilla E.R., De la Torre A.G., León-Reina L., Aranda M.A.G., Rietveld quantitative phase analysis of Yeelimite-containing cements, Cem. Concr. Res. 42 (2012) 960-971.

(13) Zajac M., Skocek J., Bullerjahn F., Ben Haha M., Effect of Retarders on the Early Hydration of Calcium-Sulpho-Aluminate (CSA) Type Cements, Cem. Concr. Res. 84 (2016) 62-75.

(14) Winnefeld F., Barlag S., Calorimetric and thermogravimetric study on the influence of calcium sulfate on the hydration of ye'elimite, J. Therm. Anal. Calorim. 101 (2010) 949-957.

(15) Hargis C.W., Kirchheim A.P., Monteiro P.J.M., Gartner E.M., Early age hydration of calcium suloaluminate (synthetic ye'elimite, $C_4A_3\underline{S}$) in the presence of gypsum and varying amounts of calcium hydroxide, Cem. Concr. Res. 48 (2013) 105-115.

(16) Promentilla M.A.B., Sugiyama T., Hitomi T., Takeda N., Quantification of tortuosity in hardened cement pastes using synchrotron-based X-ray computed microtomography, Cem. Concr. Res. 39 (2009) 548-557.

(17) Bossa N., Chauranda P., Vicented J., Borschnecka D., Levarda C., Aguerre-Chariol O., Rosea J., Micro- and nano-X-ray computed-tomography: A step forward in the characterization of the pore network of a leached cement paste. Cem. Concr. Res. 67 (2015) 138-147.

(18) Gallucci E., Scrivener K., Groso A., Stampanoni M., Margaritondo G., 3D Experimental investigation of the Microstructure of Cement Pastes Using Synchrotron X-ray Microtomography (μCT), Cem. Concr. Res. 37 (2007) 360-368.

(19) Gastaldi D., Canonico L., Capilli E., Boccaleri M., Milanesio L., Palin G., Croce F., Marone K., Mader K., Stampanoni M., In Situ Tomographic Investigation on the Early Hydration Behaviours of Cementing Systems, Constr. Build. Mater. 29 (2012) 284-290.

(20) Adrien J., Meille S., Tadier S., Maire E., Sasaky L., In-situ X-ray tomographic monitoring of gypsum plaster setting, Cem. Concr. Res. 82 (2016) 107-116.

(21) Aranda M.A.G., Recent Studies of Cements and Concretes by Synchrotron Radiation Crystallographic and Cognate Methods, Crystallography Reviews 22 (2016) 150-196.

(22) Dierolf M., Menzel A., Thibault P., Schneider P., Kewish C.M., Wepf R., Bunk O., Pfeiffer F., Ptychographic X-ray Computed Tomography at the Nanoscale, Nature 467 (2010) 436-440.

(23) Rodenburg J., Hurst A.C., Cullis A.G., Dobson B.R., Pfeiffer F., Bunk O., David C., Jefimovs K., Johnson I., Hard X-rays Lensless Imaging of Extended Objects, Phys. Rev. Lett. 98 (2007) 034801.

(24) Guizar-Sicairos M., Fienup J.R., Phase Retrieval with Transverse Translation Diversity: a Nonlinear Optimization Approach, Opt. Express 16 (2008) 7264-7278.

(25) Thibault P., Dierolf M., Bunk O., Menzel A., Pfeiffer F., Probe Retrieval in Ptychographic Coherent Diffractive Imaging, Ultramicroscopy 109 (2009) 338-343.

(26) Faulkner H.M.L., Rodenburg J.M., Movable Aperture Lensless Transmission Microscopy: a Novel Phase Retrieval Algorithm, Phys. Rev. Lett. 93 (2004) 023903.

(27) Holler M., Diaz A., Guizar-Sicairos M., Karvinen P., Färm E., Härkönen E., Ritala M., Menzel A., Raabe J., Bunk O., X-ray Ptychographic Computed Tomography at 16 nm Isotropic 3D Resolution, Sci. Rep. 4 (2014) 3857.

(28) Diaz A., Trtik P, Guizar-Sicairos M., Menzel A., Thibault P., Bunk O., Quantitative X-ray Phase Nanotomography, Phys. Rev. B 85 (2012) 020104.

(29) Trtik P., Diaz A., Guizar-Sicairos M., Menzel A., Bunk O., Density Mapping of Hardened Cement Paste Using Ptychographic X-ray Computed Tomography, Cem. Concr. Comp. 36 (2013) 71-77.

(30) da Silva J.C., Trtik P., Diaz A., Holler M., Guizar-Sicairos M., Raabe J., Bunk O., Menzel A., Mass Density and Water Content of Saturated Never-Dried Calcium Silicate Hydrates, Langmuir 31 (2015) 3779-3783.

(31) Cuesta A., De la Torre A.G., Santacruz I., Trtik P., da Silva J.C., Diaz A., Holler M., Aranda M.A.G., Chemistry and Mass Density of Aluminum Hydroxide Gel in Eco-Cements by Ptychographic X-ray Computed Tomography J. Phys. Chem. C, submitted (2016)

(32) Cuesta A., De la Torre A.G., Losilla E.R., Peterson V.K., Rejmak P., Ayuela A., Frontera C., Aranda M.A.G., Structure, atomistic simulations, and phase transition of stoichiometric yeelimite, Chem. Mater. 25 (2013) 1680-1687.

(33) Holler M., Raabe J., Diaz A., Guizar-Sicairos M., Quitmann C., Menzel A., Bunk O., An instrument for 3D X-ray nano-imaging, Rev. Sci. Instrum. 83 (2012) 073703.

(34) Holler M., Raabe J., Error motion compensating tracking interferometer for the position measurement of objects with rotational degree of freedom, Optical Engineering (2015) 054101.

(35) Gorelick S., Vila-Comamala J., Guzenko V.A., Barrett R., Salomé M., Davida C., High-Efficiency Fresnel Zone Plates for Hard X-Rays by 100 keV e-beam Lithography and Electroplating, J. Synchrotron Rad. 18 (2011) 442-448.

(36) Dinapoli R., Bergamaschi A., Henrich B., Horisberger R., Johnson I., Mozzanica A, Schmid E., Schmitt B., Schreiber A., Shi X., Theidel G., EIGER: next generation single photon counting detector for X-ray applications, Nucl. Instrum. Methods. Phys. Res. A 650 (2011) 79-83.

(37) da Silva J.C., Menzel A., Elementary signals in ptychography, Opt. Express 23 **(**2015) 33812-21.

(38) Edo T.B., Batey D.J., Maiden A.M.. Rau C., Wagner U., Pešić Z.D., Waigh T.A., Rodenburg J.M., Sampling in x-ray ptychography, Phys. Rev. A 87 (2013) 053850.

(39) Huang X., Yan H., Harder R., Hwu Y., Robinson I.K., Chu Y.S., Optimization of overlap uniformness for ptychography, Opt. Express 22 (2014) 12634-12644.

(40) Kaestner A., Munch B., Trtik P., Spatio-temporal Computed Tomography of Dynamic Processe, Opt. Eng. 50 (2011) 123201.

(41) Thibault P., Dierolf M., Bunk O., Menzel A., Pfeiffer F., Probe retrieval in ptychographic coherent diffractive imaging, Ultramicroscopy 109 (2009) 338-343.

(42) Goldstein R.M., Zebker H.A., Werner C.L., Satellite Radar Interferometry: Two-Dimensional Phase Unwrapping, Radio Sci. 23 (1988) 713-720.

(43) Thibault P., Guizar-Sicairos M., Maximum-likelihood refinement for coherent diffractive imaging, New. J. Phys. 14 (2012) 063004.

(44) Guizar-Sicairos M., Diaz A., Holler M., Lucas M.S., Menzel A., Wepf R.A., Bunk O., Phase Tomography from X-Ray Coherent Diffractive Imaging Projections, Opt. Express 19 (2011) 21345-21357.

(45) Guizar-Sicairos M., Boon J.J., Mader K., Diaz A., Menzel A., Bunk, O., Quantitative interior x-ray nanotomography by a hybrid imaging technique, Optica 2 (2015) 259-266.

(46) Van Hell M., Schatz M., Fourier shell correlation threshold criteria, J. Struct. Biol. 151 (2005) 250-262.

(47) Abramoff M.D., Magalhaes P.J., Ram, S.J., Image processing with ImageJ, J. Biophotonics Int. 11 (2004) 36-42.

(48) Schindelin J., Arganda-Carreras I., Frise E., Kaynig V., Longair M., Pietzsch T., Preibisch S., Rueden C., Saalfeld S., Schmid B., Tinevez J.Y., White D.J., Hartenstein V., Eliceiri K., Tomancak P., Cardona A., Fiji: an open-source platform for biological image analysis, Nat. Methods 9 (2012) 676-682.